ORIGINAL ARTICLE

R. Pasquetti · E. Séverac · E. Serre · P. Bontoux · M. Schäfer

From stratified wakes to rotor–stator flows by an SVV–LES method

Abstract We extend a large-eddy simulation (LES) methodology, based on using the spectral vanishing viscosity (SVV) method to stabilize spectral collocation approximations, from the Cartesian to the cylindrical geometry. The capabilities of the SVV–LES approach are illustrated for two very different physical problems: (1) the influence of thermal stratification on the wake of a cylinder, and (2) the instabilities that develop in transitional and fully turbulent rotor–stator flows.

Keywords Large-eddy simulation · Spectral vanishing viscosity · Wake flows · Rotor–stator flows

PACS 47.27.ep · 47.27.E · 47.27.wb · 47.32.Ef

1 Introduction

Thanks to the huge efforts made during the three last decades several routes are now defined to achieve large-eddy simulations (LES) of complex flows. Thus one can discern the Smagorinsky subgrid-scale (SGS) model, the spectral viscosity approach, the scale similarity model, the approximate deconvolution method, etc., all of which in both their native or dynamic versions, and also the so-called monotonicity integrated LES (MILES) approaches (see, e.g., [4,11,14,23,39] and references therein).

The spectral vanishing viscosity (SVV) method, first introduced to handle hyperbolic one-dimensional (1D) problems with spectral methods [27,47], was introduced more recently in the LES field [19,20]. At the same time we used this approach as a stabilization technique of an approximate deconvolution method (ADM) [45,46] (see also [10,12]) of the SGS tensor [29], but with a different multidimensional extension of the initial 1D SVV method. The SVV method is of major interest in the field of spectral, spectral element, or hp-finite element methods [21], because it allows one to stabilize the computations without losing the basic exponential convergence property of these spectral methods. Stabilization is achieved by completing the momentum, and eventually combined transport–diffusion equations, with SVV terms. Some problems remain, concerning, e.g., near-wall modeling (NWM) when the Reynolds number is so high that the boundary layers cannot be resolved by the mesh [36]. Note that, despite the fact that using high-order methods for LES has the advantage

---

Communicated by R.D. Moser

R. Pasquetti (✉)
Laboratoire J.A. Dieudonné, UMR CNRS 6621, Université de Nice-Sophia Antipolis, Sophia Antipolis, France
E-mail: richard.pasquetti@unice.fr

E. Séverac · E. Serre · P. Bontoux
Laboratoire MSNM-GP, UMR CNRS 6181, Universités d'Aix-Marseille, Marseille, France

M. Schäfer
Fachgebiet Numerische Berechnungverfahren im Maschinenbau, Technische Universität Darmstadt, Darmstadt, Germany

of avoiding mixing between approximation errors and SGS modeling, work in this field remains rare, see, e.g., [5,18]. Note also that the SVV method could be regarded as an SGS model, but that this link between a stabilization technique and a physical modeling remains to be addressed.

In recent papers we have largely developed the SVV approach for LES, i.e., the SVV-LES approach [20]. Thus, comparisons between the SVV–LES and an ADM-stabilized SVV may be found in [30]; a sensitivity study of SVV–LES results to the SVV control parameters is carried out in [31]; a formulation of the method in weak form, for spectral element approximations, is proposed in [49]; and a unified strong–weak approach with comparisons to experimental data is given in [32]; details of the computation of the dissipation rates may be found in [33]. The computational results have essentially been obtained for the turbulent wake of a cylinder, but additional results for rotor–stator flows have also been described [44].

Here we want to point out that the SVV–LES approach may apply to various physical problems, such as stratified wakes and rotor–stator flows. Although such flows are very different, our spectral numerical approaches are similar, except that for rotor–stator flows the SVV method is used in the cylindrical coordinate system. This extension of our previous works, developed in Cartesian geometry, is addressed in Sect. 2, where we describe an original formulation of the SVV method for the Navier–Stokes equations in cylindrical coordinates. The capabilities of the SVV–LES modeling are illustrated in Sects. 3 and 4. In Sect. 3 the SVV–LES method is used to show the influence of thermal stratification on the spatial development of wakes and in Sect. 4 to compute rotor–stator flows both in transitional laminar–turbulent and fully turbulent regimes. We conclude in Sect. 5.

2 SVV implementation and numerical method

Basically, the SVV method relies on the introduction of a discretization-dependent artificial diffusive term only active in the highest frequency range of the numerical approximation. For 1D partial differential equations, with N being the discretization parameter and $u_N(x)$ the numerical solution, such an additional term reads:

$$V_N \equiv \epsilon_N \partial_x (Q_N(\partial_x u_N)), \tag{1}$$

where ϵ_N is an $O(1/N)$ coefficient and Q_N is the spectral viscosity operator such that, in the 1D nonperiodic case [27] and with $\{L_k\}_{k\geq 0}$ for the set of the Legendre polynomials,

$$\forall \phi, \quad \phi = \sum_{k=0}^{\infty} \hat{\phi}_k L_k, \quad Q_N \phi \equiv \sum_{k=0}^{N} \hat{Q}_k \hat{\phi}_k L_k$$

where $\hat{Q}_k = 0$ if $k \leq m_N$ and $1 \geq \hat{Q}_k > 0$ if $N \geq k > m_N$, with e.g., $m_N = \sqrt{N}$ and $\hat{Q}_k = \exp(-(k-N)^2/(k-m_N)^2)$. In the periodic case trigonometric polynomials are substituted for the Legendre polynomials. In the framework of collocation Chebyshev methods we use a similar definition, but with Chebyshev instead of Legendre polynomials. The main point is of course that a hierarchical basis must be used. Note that theoretical papers use a step variation rather than the smoother exponential dependence of $\hat{Q}_k$, which is commonly used in applications.

Extending the definition (1) to a multidimensional context is not as natural as it appears when looking at the different forms proposed in the literature, see e.g., [7,17,19]. For us, we advocate the following definition:

$$V_N \equiv \nabla \cdot (\epsilon_N Q_N(\nabla u_N)) \tag{2}$$

where

$$\epsilon_N Q_N \equiv \text{diag}\{\epsilon_{N_i} Q_{N_i}^i\},$$

where $Q_{N_i}^i$ is the 1D viscosity operator acting in direction i. Thus, we actually use a diagonal matrix form of the operator $\epsilon_N Q_N$, just as one introduces a nonscalar diffusivity when anisotropic media are considered. Note that such a 3D extension is not trivial, thus:

– Contrarily to some authors, see e.g., [21], we have not introduced a multidimensional spectral viscosity operator. Our approach only makes use of the 1D operator in each spatial direction, so that if the SVV is only required in one direction, say in the x-direction, no SVV is introduced in the y- and z-directions. This is possible when using a multidimensional basis resulting from the tensorial product of 1D bases [see [49] for (quadrangular) spectral elements]. This is however not possible when unstructured meshes are considered, as in [21] for hp-finite elements.

– If a mapping $f : \hat{\Omega} \to \Omega$ from the reference domain $\hat{\Omega}$ to the physical domain Ω is involved, then we use:

$$\epsilon_N Q_N (\nabla u_N) \equiv \epsilon_N Q_N \left(\hat{\nabla}(u_N \circ f) \right) G, \tag{3}$$

where G is the Jacobian matrix of f^{-1} and $\hat{\nabla}$ denotes the gradient with respect to the variables of the reference domain. The polynomial approximation indeed holds in the reference domain, i.e., for the function $u_N \circ f$. For a different approach, where the SVV contribution is governed by the gradient in the physical domain rather than in the computational one, see e.g., [21].

In the framework of collocation methods the SVV stabilization can be simply implemented by combining the diffusion and SVV terms to obtain

$$a\Delta_{\text{SVV}} u_N \equiv a\Delta u_N + \nabla \cdot \epsilon_N Q_N(\nabla u_N) = a\nabla \cdot S_N(\nabla u_N), \tag{4}$$

where a is a dimensionless transport coefficient and where

$$S_N = 1 + \frac{\epsilon_N}{a} Q_N.$$

It may be observed that the SVV and effective viscosities appear to be disconnected and some authors have tried to preserve a link between them [20]. However, this is typical of most LES approaches, especially those based on an SGS viscosity, e.g., the celebrated Smagorinsky model. When looking at the dissipation rate of the turbulent kinetic energy, it is certainly desirable to maintain a nonnegligible value of the viscous part with respect to the SGS (here the SVV) part, by refinement, if necessary, of the computational grid [13,33]. The determination of the correct values for the SVV parameters, ϵ_N and m_N, is discussed in [31]. In this paper we suggest, on the basis of numerical experiments, to simply minimize the magnitude of the SVV stabilization term.

Now, with $\partial_i \equiv \partial_{x_i}$, if we denote

$$\tilde{\partial}_i \equiv S_{N_i}^i \partial_i, \quad S_{N_i}^i = 1 + \frac{\epsilon_{N_i}}{a} Q_{N_i}^i$$

we simply have

$$\Delta_{\text{SVV}} = \sum_i \partial_i \tilde{\partial}_i. \tag{5}$$

In a multidimensional context such a formulation of the SVV Laplacian operator is strongly linked to our definition of the operator $\epsilon_N Q_N$. It enables an efficient implementation of the SVV method: differences between a direct numerical simulation (DNS) and a LES only occur in the preliminary part of the computation, when the SVV modified operators are setup.

Our goal now is to establish a similar formulation for the cylindrical coordinate system used for rotor–stator flows. In the cylindrical system (r, θ, z), we also use the definition (2) of the SVV term to obtain:

$$\Delta_{\text{SVV}} = \partial_r \tilde{\partial}_r + \frac{1}{r} \tilde{\partial}_r + \frac{1}{r^2} \partial_\theta \tilde{\partial}_\theta + \partial_z \tilde{\partial}_z. \tag{6}$$

The natural periodicity of the azimuthal direction motivates the use of Fourier expansions. For the k-Fourier mode and with $\hat{S}_k^\theta$ for the corresponding coefficient of the θ-SVV operator, this yields the SVV Laplacian operator:

$$\Delta_{\text{SVV},k} = \partial_r \tilde{\partial}_r + \frac{1}{r} \tilde{\partial}_r - \frac{\hat{S}_k^\theta}{r^2} k^2 + \partial_z \tilde{\partial}_z. \tag{7}$$

For the Navier–Stokes equations one must implement the vector Laplacian operator. This is a trivial task in the Cartesian system, because the vector Laplacian splits into scalar Laplacian applied to each vector component. A difficulty with the cylindrical coordinate system comes from the fact that the vector Laplacian is not diagonal. An efficient way to recover a diagonal operator is the transformation [35]:

$$v_+ = v_r + \mathrm{i}v_\theta, \qquad v_- = v_r - \mathrm{i}v_\theta \quad (\mathrm{i}^2 = -1), \tag{8}$$

where $\boldsymbol{v}$ is any vector function. Then, in the $(\boldsymbol{e}_+, \boldsymbol{e}_-, \boldsymbol{e}_z)$ basis the vector Laplacian operator reads:

$$\nabla^2 = \mathrm{diag}\left\{\Delta - \frac{1}{r^2} + \frac{2\mathrm{i}}{r^2}\partial_\theta, \Delta - \frac{1}{r^2} - \frac{2\mathrm{i}}{r^2}\partial_\theta, \Delta\right\}, \tag{9}$$

where we have used ∇^2 and Δ to represent the vector and scalar Laplacian, respectively. For the k-Fourier mode one obtains:

$$\nabla_k^2 = \left(\partial_{rr} + \frac{1}{r}\partial_r + \partial_{zz}\right)\mathbb{I} - \frac{1}{r^2}\mathrm{diag}\left\{(k+1)^2, (k-1)^2, k^2\right\}, \tag{10}$$

where $\mathbb{I}$ is the identity matrix.

The expression for the corresponding SVV vector Laplacian operator follows:

$$\nabla_{\mathrm{SVV},k}^2 = \left(\partial_r\tilde\partial_r + \frac{1}{r}\tilde\partial_r + \partial_z\tilde\partial_z\right)\mathbb{I} - \frac{\hat{S}_k^\theta}{r^2}\mathrm{diag}\left\{(k+1)^2, (k-1)^2, k^2\right\}. \tag{11}$$

Another difficulty of the cylindrical system comes from the singularity of the Laplacian operator at the axis (see e.g., [2,3,28,43]). We do not address the problem here, since for the rotor–stator flows considered in this paper the flow is in fact computed in a ring.

Let us conclude this Section by mentioning the main features of the two codes that have been developed using this SVV–LES methodology. More details may be found in [8,30,32,34] for the Cartesian code and in [38,43] for the cylindrical code.

- The time scheme is second-order accurate: second-order backward differences are used for the approximation of the time derivative of the velocity (and eventually of the temperature).
- The SVV modified diffusion terms are treated implicitly.
- The convective terms are treated explicitly. A second-order Adams–Bashforth extrapolation is used in the cylindrical code whereas an operator integration factor semi-Lagrangian method is used in the Cartesian code.
- Projection methods are used to obtain a divergence-free velocity field. This relies on the so-called unique grid $\mathbb{P}_N - \mathbb{P}_{N-2}$ approximation in the Cartesian code whereas one uses a preliminary solve for the pressure in the cylindrical code.
- Fourier–Galerkin approximations are used in the homogeneous direction, i.e., in the spanwise and azimuthal directions for the Cartesian and cylindrical codes, respectively. Chebyshev collocation approximations are used in the nonhomogeneous directions.
- Specific to the Cartesian code: (1) a domain decomposition technique is used in the streamwise direction, and (2) the bluff body is modeled by using a pseudopenalization technique.

3 Stratified wakes of a cylinder

Stratified fluids are essentially characterized by the Brunt Väisälä angular frequency $\tilde{N}$, such that $\tilde{N}^2 = -g\partial_y\rho/\rho$, where y denotes the vertical axis, ρ the fluid density, and g the acceleration due to gravity. In the case of thermal stratification, if the variations of $\rho(y)$ are weak, then using α to denote the thermal expansion coefficient, $\tilde{N}^2 \approx g\alpha\partial_y T_0$, where T_0 is the temperature profile at rest. Hereafter we suppose that the stratification is linear ($\partial_y T_0 = cte > 0$). In dimensionless form, from the Brunt Väisälä angular frequency arises the internal Froude number or, equivalently, the Richardson number. Using D, U, and $\delta T = D\partial_y T_0$ to represent the characteristic length, velocity, and temperature gap, respectively, one has $F = U/(\tilde{N}D)$ and $Ri = 1/F^2$. The modeling is based on the incompressible Navier–Stokes equations coupled with a transport–diffusion equation for the temperature within the Boussinesq approximation, i.e., the density variations are only considered in the buoyancy term that appears in the momentum equation. The Boussinesq equations can be written:
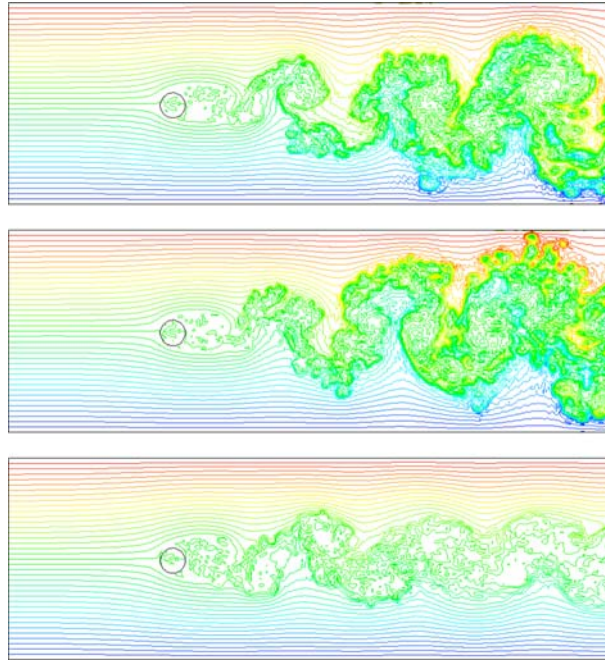
Fig. 1 Temperature field at $z = 0$: $Ri = 0$ (*top*), $Ri = 18 \times 10^{-5}$ (*middle*), and $Ri = 0.25$ (*bottom*)

$$D_t \boldsymbol{u} = -\nabla p + Ri T \boldsymbol{e}_y + \frac{1}{Re}\nabla^2 \boldsymbol{u} \tag{12}$$

$$\nabla \cdot \boldsymbol{u} = 0 \tag{13}$$

$$D_t T = \frac{1}{Pe}\Delta T \tag{14}$$

with the usual notations, t: time, D_t: material derivative, p: pressure term, $\boldsymbol{e}_y$: vertical unit vector, $\boldsymbol{u}$: velocity, T: temperature, Re: Reynolds number, and Pe: Péclet number.

SVV stabilizing terms are introduced both in the momentum and energy equations. As explained earlier, this is done by substituting SVV Laplacian for the Laplacian operators. Thus, we set $a = Re^{-1}$ for the momentum equation and $a = Pe^{-1}$ for the temperature equation in (5).

SVV–LES results obtained for the wake of a cylinder in thermally stratified water are presented. The parameters D and U here are the cylinder diameter and the fluid velocity far upstream of the cylinder, respectively. The cylinder is embedded in a channel-like geometry and the spanwise direction is assumed homogeneous. The inlet velocity is U, free-slip boundary conditions are assumed at the horizontal boundaries and an advection condition at the velocity U is enforced at the outlet. For the temperature a constant profile is enforced at the inlet, adiabaticity is assumed at the horizontal boundaries, and an advection condition is also used at the outlet. Three cases are investigated, corresponding to Richardson numbers of $Ri = 0$, $Ri = 18 \times 10^{-5}$, and $Ri = 0.25$. In the former case the temperature behaves like a passive scalar whereas for $Ri \neq 0$ there is a thermal-hydrodynamic coupling. In all cases the Reynolds and Prandtl numbers are $Re = 3900$ and $Pr = 7$, so that $Pe = Pr Re = 27300$. Note that for $Ri = 0$ comparisons with experiments are given and discussed in [32]. The computational domain is $\Omega = (-6.5, 17.5) \times (-4, 4) \times (-2, 2)$, and the cylinder is centered at $x = y = 0$. The discretization parameters are the following: five subdomains with $61 \times 121 \times 60$ grid points in each of them, and a time step of $\Delta t = 5 \times 10^{-3}$. The SVV parameters are $m_N = N/2$ and $\epsilon_N = 1/N$, with $N = (60, 120, 30)$.

Instantaneous fields: The instantaneous temperature fields, see Fig. 1, clearly show the turbulent features of the flow. Essentially one observes that such fields are similar for $Ri = 0$ and $Ri = 18 \times 10^{-5}$, whereas for $Ri = 0.25$ one observes the expected confinement effect due to the stratification, see e.g., [6].

Mean flow: Figure 2 shows the mean profiles of the streamwise component of the velocity. These profiles are averaged in time and also in the z-spanwise direction. On the left one has $< u_x > (y)$ for $x \approx 7$, whereas on the right one has $< u_x > (x)$ for $y = 0$. Again one observes the influence of the stratification for $Ri = 0.25$,
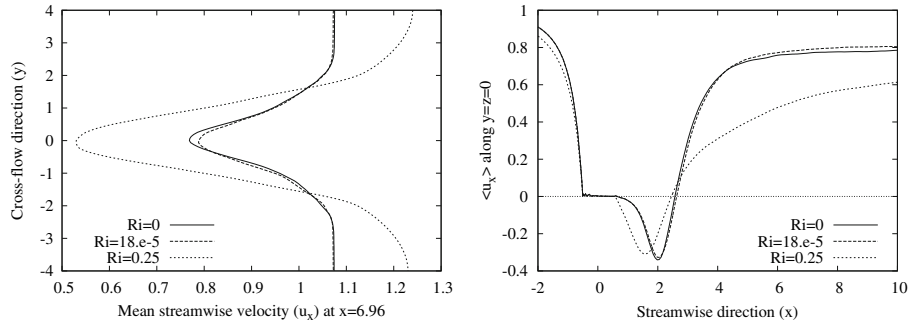
Fig. 2 For $Ri = \{0, 18 \times 10^{-5}, 0.25\}$, $< u_x > (y)$ at $x \approx 7$ (*left*) and $< u_x > (x)$ at $y = 0$ (*right*)
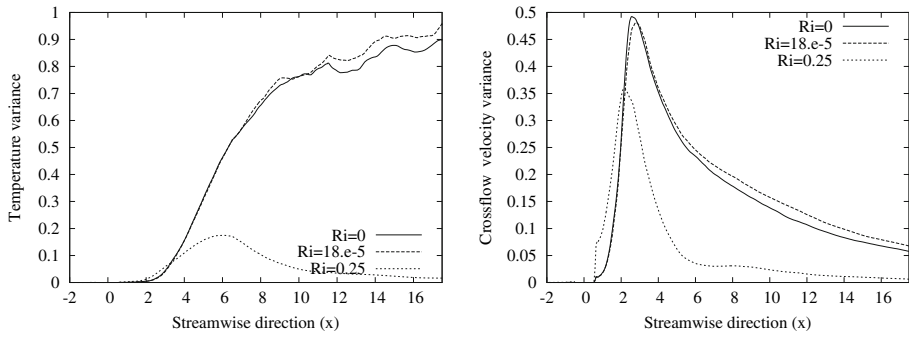
Fig. 3 For $Ri = \{0, 18 \times 10^{-5}, 0.25\}$, $< T'^2 > (x)$ (*left*) and $< u_y'^2 > (x)$ (*right*) at $y = z = 0$ (superscript prime represents deviation from the mean value)

whereas the results obtained for $Ri = 18 \times 10^{-5}$ and $Ri = 0$ are very similar. We also observe the influence of the stratification on the recirculation length, which is shorter for $Ri = 0.25$.

Temperature and crossflow velocity variances: The influence of the stratification is especially obvious when looking at the variations in streamwise direction of the temperature and crossflow velocity variances, see Fig. 3. The blocking effect due to the stratification is especially evident in the temperature results, since the temperature variance shows a maximum for $x \approx 6$ if $Ri = 0.25$, whereas this maximum is not reached at the outlet of the computational domain for $Ri = 0$ and $Ri = 18 \times 10^{-5}$. For the Reynolds shear stress, one observes a shift of the maximum towards the near wake and a quicker decrease beyond this maximum for the stronger stratification.

Drag and lift coefficients: The pseudopenalization technique used to model the bluff body allows an efficient computation of the drag and lift coefficients, by numerical integration of the penalty term (implicitly) introduced to cancel the velocity inside the obstacle. However, although satisfactory results have been obtained for the DNS of the 2D wake of a cylinder at Reynolds number $Re = 200$ [34], here these coefficients are found to be overestimated (nonstratified case), probably due to a lack of resolution in the near-wall region. Work is presently being carried out to clarify this point.

4 Rotor–stator flow

We now investigate a rotor–stator flow within a cavity made of two discs enclosing an annular domain of radial extent $\Delta R = R_1 - R_0$, where R_0 and R_1 are the internal and external radii, respectively. Two stationary cylinders of height H, termed the shaft and the shroud, bound the domain, see Fig. 4. Two parameters define the shape of the system: These may be taken as the curvature parameter $R_m = (R_0 + R_1)/\Delta R$ and the aspect ratio $L = \Delta R/H$. Here, $R_m = L = 5$. The reference time and velocity are Ω^{-1} and ΩR_1, respectively, and the Reynolds number is defined as $Re = \Omega R_1^2/\nu$, where ν is the kinematic viscosity.

The normalized dimensionless coordinates in any meridian plane are $(r = r_{\text{dim}}/\Delta R - R_m, z = 2z_{\text{dim}}/H - 1) \in [-1, 1]^2$ (r_{dim} and z_{dim} are the corresponding dimensioned variables). No-slip boundary conditions are applied to all walls: $u_r = u_\theta = u_z = 0$, except on the rotating disk ($z = 1$), where $u_\theta = (R_m + r)/(R_m + 1)$. The junction of the stationary cylinders with the rotor is regularized by employing a boundary layer function,
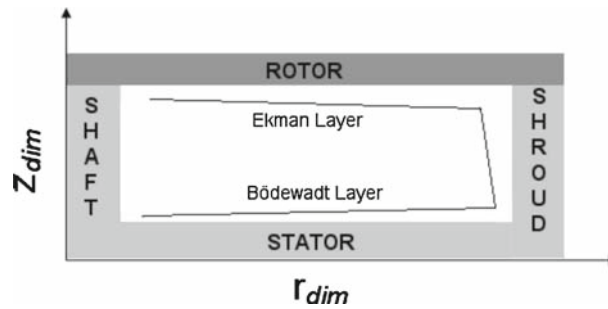
Fig. 4 Schematic of the rotor–stator cavity

$u_\theta = \exp(-(z-1)/\mu)$, where the value of the shape parameter $\mu = 6 \times 10^{-3}$ provides a reasonable representation of experimental conditions (there is a thin gap between the edge of the rotating disc and the stationary sidewall), while retaining spectral accuracy.

Rotor–stator flows are very challenging for numerical modeling, particularly in turbulent regimes, see e.g., [24–26,48]. A characteristic feature of such flows is indeed the coexistence of adjacent coupled flow regions involving laminar, transitional, and turbulent regions which are completely different in terms of their flow characteristics. Moreover, the turbulence is strongly inhomogeneous and anisotropic because of confinement, flow curvature, and rotational effects. At present, computer performance only permits DNS of transitional laminar–turbulent cavity flows ($Re \approx 10^5$) [41]. Due to the coexistence of diverse flow regimes, attempts to compute turbulent rotor–stator flows by using statistical approaches, i.e., based on the Reynolds-averaged Navier–Stokes equations, are rather disappointing. Second-order closures could be more appropriate [22,37], but even if they provide a correct localization of the laminar and turbulent regions, the Reynolds stresses are not fully satisfactory, particularly near the rotating disc. Consequently, the LES approach is a valuable approach to the computation of such flows. As far as we are aware, efficient LES of fully turbulent flows in an enclosed rotor–stator cavity have not yet been performed. However, one should mention the work of Andersson and Lygren [1] who performed wide- and narrow-gap simulations for $Re \leq 1.6 \times 10^6$, but using a simplified model in which the flow is restricted to an angular section of the cavity and is homogeneous in the radial direction.

Firstly, a SVV–LES simulation is presented for a transitional flow regime at moderate Reynolds number ($Re = 7 \times 10^4$) and comparisons with a reference DNS solution are provided. Further, a much higher Reynolds number flow, $Re = 10^6$, is computed to show the capability of the SVV technique to investigate the turbulence features of such flows.

4.1 Transitional rotor–stator flow

At $Re = 10^4$ the rotor–stator flow is steady, axisymmetric, and consists of two distinct boundary layers (at the discs) and of a central core flow in near solid body rotation. Using this flow as an initial condition, the Reynolds number was increased step by step up to $Re = 7 \times 10^4$. According to previous numerical and experimental works [40,41] the flow is then transitional laminar–turbulent, with a fully turbulent stator layer while the rotor layer remains laminar.

DNS computations were performed on a thin grid of $101 \times 200 \times 65$ points in the (r, θ, z) directions, respectively, in order to ensure aliasing-free spectra in all directions. The time step was $\Delta t = 5 \times 10^{-4}$. For the SVV–LES calculations, the grid was $33 \times 64 \times 23$ (which only represents 3.70% of the DNS resolution), with a time step of $\Delta t = 4 \times 10^{-3}$. The SVV parameters were chosen as $\epsilon_N = 2/N$ and $m_N = N/2$ in each direction, where $N = (32, 32, 22)$.

We define the wall unit value $z^+ = h_z V_\tau / \nu$, where h_z is the size of the smallest computational cell in the axial direction and V_τ is the total friction velocity at the discs. The universal value of the viscous sublayer thickness being close to five wall units, z^+ needs to be close to 1 to ensure an accurate description of the sublayer. Thanks to the accumulation of the Gauss–Lobatto grid points at the end points, for the DNS it turns out that the z^+ values are smaller than 0.2 along the discs. For the SVV–LES, we obtain larger but still reasonable values of z^+, since they remain essentially smaller than 1.4, see Fig. 5.

The flow perturbations are measured primarily by the magnitude of the axial component of velocity, which varies around a zero mean. The DNS and SVV–LES solutions show spatial structures in the stator boundary
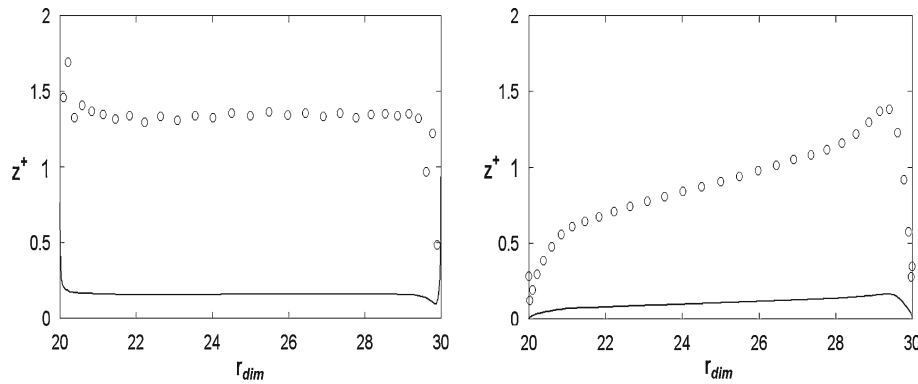
Fig. 5 Radial variation of the wall-normal value z^+ at the rotor (*left*) and at the stator (*right*) for $Re = 7 \times 10^4$. *Bold line* DNS with grid $101 \times 200 \times 65$. *Circles* SVV–LES with grid $33 \times 64 \times 23$
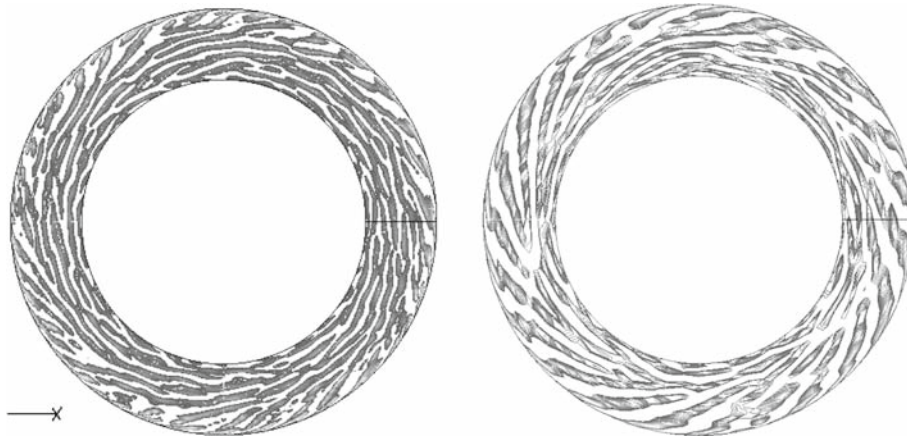

Fig. 6 Isolines of the velocity axial fluctuations in the stator boundary layer, $Re = 7 \times 10^4$. DNS result with a $101 \times 200 \times 65$ mesh (*left*) and SVV–LES result with a $33 \times 65 \times 23$ mesh (*right*)

layer corresponding to traveling vortices, which expand in rings and then in spirals in the azimuthal direction, depending on the radius, see Fig. 6. From the DNS results, one can observe four pairs of rolls in the radial direction, with a radial wavelength $12 \leq \lambda_r/\delta_B \leq 18$, where $\lambda_r = \Delta R/n$, with n being the number of rolls and $\delta_B = (\nu/\Omega_f)^{0.5}$ a characteristic length of the boundary layer, and where Ω_f denotes the angular velocity of the geostrophic core region. These rolls expand in the azimuthal direction in the spiral arms, rotating in the direction of the mean flow driven by the rotor. The vortices are advected by the mean flow to the inner radius and the spiral arms are broken, showing dislocation phenomena. The positive angle ϵ of the spiral wavefront with the geostrophic flow slightly decreases when the radius increases over the range $[5°; 22°]$, and the spiral arms turn into nearly annular flow next to the shaft. The corresponding wavelengths vary over the range $15 \leq \lambda/\delta_B \leq 28.5$, with $\lambda = 2\pi r \sin \epsilon/n$. Note that the value of the azimuthal wavenumber at large radius is almost a third times smaller in the SVV–LES solution (23 spiral arms) than in the DNS solution (37 spiral arms). This results from the small number of azimuthal modes used for the SVV–LES (maximum wavenumber 32) to correctly capture the physics of the flow in this direction, since the azimuthal wavelength of the spiral pattern is smaller than the LES azimuthal grid step.

These spiral patterns have already been observed in experiments by Schouveiler et al. [40] at $Re = 2 \times 10^4$, $R_1/H = 8.75$: the spirals patterns (noted RS1) evolve close to the shroud with an angle of about $\epsilon = 25°$, in good agreement with the structures obtained in the present computations. The main characteristics of these structures are in good agreement with those obtained by linear stability analysis for the type I instability [42].

The instantaneous data have been averaged both in time and in the homogeneous azimuthal direction. The mean flow has the same structure found in the laminar regime, with two separated boundary layers. On average, there exists a main flow in the azimuthal direction coupled with a secondary flow in the meridian plane. The core in solid body rotation can be characterized by $K = u_\theta/\Omega r_{\text{dim}}$, which measures somehow the ratio between
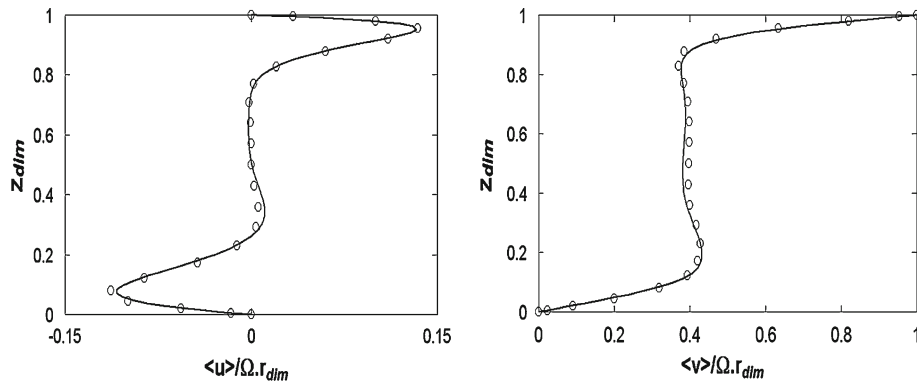
Fig. 7 Axial profiles of the radial (*left*) and tangential (*right*) components of the mean velocity at mid-radius, $Re = 7 \times 10^4$. *Bold line* DNS with grid $101 \times 200 \times 65$. *Circles* SVV–LES with grid $33 \times 64 \times 23$. Results are normalized by the local velocity of the rotor Ωr_{dim}
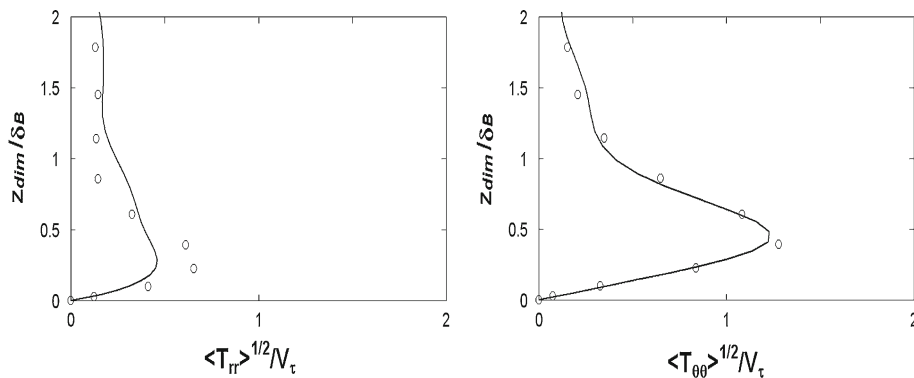

Fig. 8 Axial profiles of the radial (*left*) and tangential (*right*) normal Reynolds stresses in the stator boundary layer at the mid radius, $Re = 7 \times 10^4$. Results are normalized by the wall friction velocity, V_τ, on the stator. *Bold line* DNS with grid $101 \times 200 \times 65$. *Circles* SVV–LES with grid $33 \times 64 \times 23$

the convective terms and the Coriolis force. The differences in the thickness and shape of the radial velocity profiles near the two discs suggests that the stator layer is turbulent while the rotor layer remains laminar. This is the primary reason that in both solutions (DNS and SVV–LES) the core circumferential velocity is only about one third of that of the rotor at the same radius. DNS results provide $K = 0.3847$ at the mid radius while the SVV–LES gives $K = 0.3961$.

The radial mean velocity is very well predicted by the SVV–LES solution, see Fig. 7. In particular, both the Bödewadt (at the stator) and Ekman (at the rotor) boundary layers are very well captured. The Reynolds stresses confirm the presence of a turbulent stator layer and a laminar rotor layer (see Fig. 8) where the square roots of the radial and azimuthal normal Reynolds stresses, normalized by the wall friction velocity V_τ at the stator, are shown versus z_{dim}/δ_B. The agreement between the DNS and SVV–LES solutions appears good for the tangential normal stress, but is less satisfactory for the radial one, with a much steeper behavior of the axial profile for the SVV–LES result.

Remark There is a very strong anisotropy of the normal stresses, typical of low-Reynolds-number wall flows. As would be inferred from a stress budget, the normal stress is the greatest in the azimuthal direction, exceeding by a factor of at least 7 in DNS those in the two other directions. The maximum of the square root of the normal Reynolds stresses at the mid radius in the radial and azimuthal directions, 1.25 and 3.34, respectively, are much larger than the ones given by the experimental results of Itoh [15] by a factor of about 1.5: Itoh found maxima equal to 1.4 and 2.1, respectively, at $Re = 6.4 \times 10^5$. Nevertheless, the values obtained here are in good agreement with the axisymmetric DNS results (1.5 and 3.6 at $Re = 10^5$) obtained by Jacques and Le Quéré [16]. The difference from the experimental data can be explained by the difference between the Reynolds numbers in the present computations ($Re = 7 \times 10^4$) and in Itoh's experiment ($Re = 6.4 \times 10^5$). It is well known that an increase in the rotation rate leads to a broader range of turbulent scales and to a progressive reduction in turbulence intensities with a lower level of anisotropy between
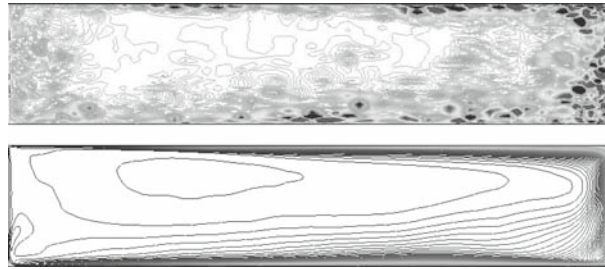
Fig. 9 Isolines of the instantaneous fields of Q-criterion for $\theta = \pi/4$ (*top*) and θ-averaged turbulent kinetic energy (*bottom*), $Re = 10^6$

components [26]. The same features have long been known in plane channel flow too. As expected, an examination of the off-diagonal Reynolds stresses shows that the normal stresses are dominant in the vicinity of the stator layer.

4.2 Turbulent rotor–stator flow

The efficiency of our SVV–LES approach has been evaluated at the much higher Reynolds number of $Re = 10^6$. The computational grid was kept relatively coarse for this Reynolds number with $81 \times 160 \times 81$ points in the (r, θ, z) directions, respectively, and a time step of $\Delta t = 10^{-4}$. As a comparison, this grid is twice as coarse as that used by Andersson and Lygren [1] in their LES (case D study of a wide-gap cavity). However, it permits one to solve the boundary layers correctly: values of z^+ around 0.65 and less than 0.6 are found for the Ekman and Bödewadt layers, respectively. Concerning the SVV parameters, as for $Re = 7 \times 10^4$, we use $\epsilon_N = 2/N$ and $m_N = N/2$ in all directions, with $N = (80, 80, 80)$ here.

At this Reynolds number, both layers are turbulent, as shown by the isolines of the mean turbulent kinetic energy in Fig. 9. The figure provides qualitative evidence that the turbulence is mainly concentrated near the two discs. The maximum of the turbulent kinetic energy is located at the rotor–shroud junction where the flow, accelerated by the rotor, impinges on the stationary outer cylinder.

The flow consists of rather tangled co-rotating vortices which originate near the shroud and move radially inward on the stator and outward on the rotor, following the main flow direction. The growth of these vortices strongly affects not only the structure of the two disc boundary layers but also the geostrophic core. This is revealed by plotting the isolines of the Q-criterion in the meridian plane (see Fig. 9). In the vicinity of the inner and outer cylinders there is now strong mixing between both boundary layers, involving a large number of vortices of different scales. This underlines the important effects that the inner and outer cylinders have on the characteristics of the turbulence.

The axial profiles at the mid radius of the mean radial and tangential component of the velocity show sharper profiles and a larger core region than at $Re = 7 \times 10^4$ (see Fig. 10). The core rotates at $K = 0.3919$ at the mid radius, which corresponds to a local Reynolds number of $Re_{loc} = \Omega r_{dim}^2 / \nu = 694444$. This value of K is in close agreement both with the numerical work of Andersson and Lygren [1] ($K = 0.40$ at $Re_{loc} = 640000$ in their case D) and the experimental results of Itoh et al. [15] ($K = 0.41$). The small underestimation of K is mainly due to differences in the problem modeling (a cylindrical cavity for Itoh et al. [15], an homogeneous cavity in radial direction for Andersson and Lygren [1], and a shrouded rotor–stator annular cavity for the SVV–LES). Indeed, the stationary inner cylinder greatly stabilizes the flow and the shroud tends to slow the flow by dissipating a lot of energy in the impinging jet and in the Stewardson layer that follows the Ekman layer in the upper part of the shroud.

As no reference profile is available at this Reynolds number, we compared two local parameters introduced by Daily and Nece [9] based on the wall friction velocity: the skin friction drag coefficient $C_\theta = 2(V_\tau/r_{dim}\Omega)^2$ derived from the torque exerted by the fluid on the two discs and the local stress Reynolds number $Re_\tau = r_{dim}V_\tau/\nu$.

The SVV–LES calculations give values at the mid radius of the skin friction drag of $C_\theta = 1.6 \times 10^{-3}$ in the Ekman layer and $C_\theta = 8.74 \times 10^{-4}$ in the Bödewadt layer. These values are slightly smaller than those found by Andersson and Lygren [1], where $C_\theta = 2.05 \times 10^{-3}$ and $C_\theta = 1.15 \times 10^{-3}$, respectively. The relative dissipation rate between the two layers due to the skin friction, $C_\theta(rotor)/C_\theta(stator)$, is 1.83 for the
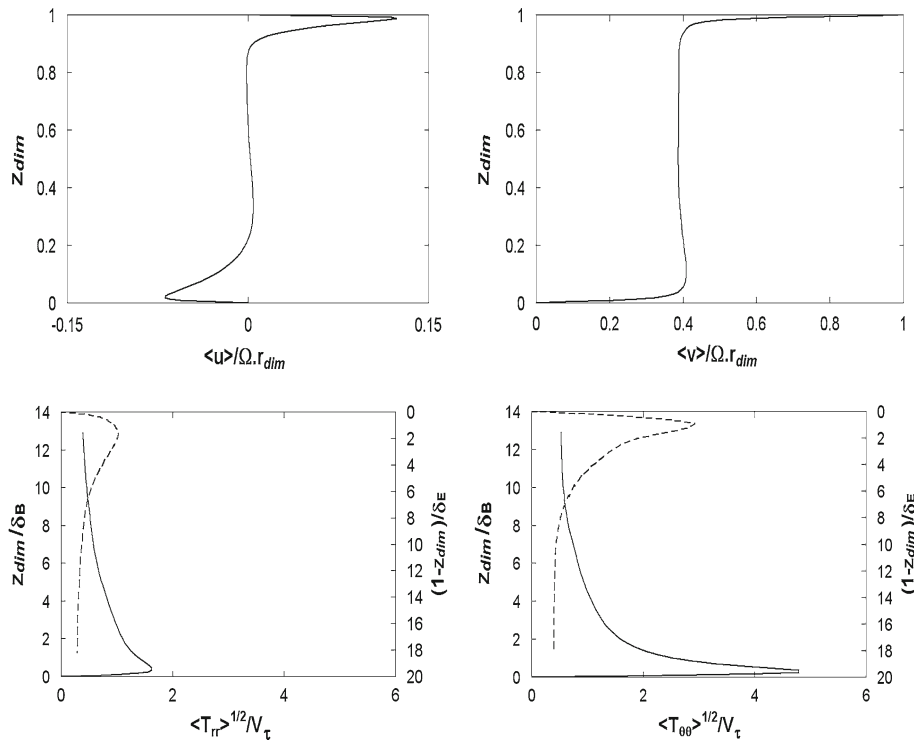
Fig. 10 Axial profiles at the mid radius of the mean radial velocity (*top left*), mean tangential velocity (*top right*), the square root of the radial (*bottom left*) and azimuthal (*bottom right*) normal Reynolds Stresses in the Ekman (*solid line*) and Bödewadt (*dashed line*) layers, $Re = 10^6$. Mean velocities are normalized by the local velocity of the rotor. The square roots of the Reynolds stresses are normalized by the local friction velocity, V_τ, on the corresponding disc

SVV–LES. This value is in close agreement with the value of 1.79 of Andersson and Lygren [1] for their case D and with the value 2 measured experimentally by Itoh et al. [15].

The local stress Reynolds numbers at the mid radius are found to be $Re_\tau = 525$ at the rotor and $Re_\tau = 288$ at the stator. These values, which show that the level of turbulence at the mid radius is larger in the Ekman than in the Bödewadt layer, are very close to those obtained by Andersson and Lygren [1]: $Re_\tau = 525$ and $Re_\tau = 284$, respectively.

5 Conclusion

Using high-order methods for the LES of complex flows is certainly of interest, especially to avoid a mixing of the approximation errors and the SGS modeling. In this spirit, the spectral vanishing viscosity (SVV) method appears to be a good candidate since it allows one to stabilize the computations while preserving the so-called spectral accuracy. Moreover, the recurrent problem of the commutation error between the filtering and differentiation operators is bypassed, even if of course it is indeed filtered values that are computed. In this paper we have extended a methodology developed in Cartesian geometry to the case of cylindrical coordinates, for spectral collocation solvers. Examples of applications to physical problems as different as stratified wake flows and rotor–stator flows have been provided. We have especially focused on rotor–stator flows in the transitional laminar–turbulent and fully turbulent regimes, with comparisons to DNS data or to other experimental and numerical investigations. For such closed rotor–stator cavity flows the present SVV–LES approach has yielded promising results.

References

1. Andersson, H.I., Lygren, M.: LES of open rotor–stator flow. Int. J. Heat Fluid Flow **27**(4), 551–557 (2006)
2. Bernardi, C., Dauge, M., Maday, Y.: Spectral Methods for Axisymmetric Domains. Elsevier, Amsterdam (1999)
3. Blackburn, H.M., Sherwin, S.J.: Formulation of a Galerkin spectral element-fourier method for three-dimensional incompressible flows in cylindrical geometries. J. Comput. Phys. **197**(2), 757–778 (2004)
4. Boris, J.P., Grinstein, F.F., Oran, E.S., Kobe, R.L.: New insights into large eddy simulation. Fluid Dyn. Res. **10**, 199–228 (1992)
5. Bouffanais, R., Deville, M.O., Fischer, P.F., Leriche, E., Weill, D.: Large-eddy simulation of the lid-driven cubic cavity flow by the spectral element method. J. Sci. Comput. **27**(1–3), 151–162 (2006)
6. Boyer, D.L., Davies, P.A., Fernando, H.J.S., Zhang, X.: Linearly stratified flow past a horizontal cylinder. Phil. Trans. R. Soc. Lond. **A 328**, 501–528 (1989)
7. Chen, G.Q., Du, Q., Tadmor, E.: Spectral viscosity approximations to multidimensional scalar conservations laws. Math. Comput. **204**, 629–643 (1993)
8. Cousin, L., Pasquetti, R.: High-order methods for the simulation of transitional to turbulent wakes. In: Lu Y., Sun W., Tang T. (eds.) Advances in Scientific Computing and Applications. Science Press, Beijing (2004)
9. Daily, J.W., Nece, R.E.: Chamber dimension effects on induced flow and frictional resistance of enclosed rotating discs. ASME J. Basic Eng. **82**, 217–232 (1960)
10. Domaradzki, J.A., Saiki, E.M.: A subgrid-scale model based on the estimation of unresolved scales of turbulence. Phys. Fluids **9**(7), 2148–2164 (1997)
11. Gatsky, T.B., Hussaini, M.Y., Lumley, J.L.: Simulation and modeling of turbulent flows. In: Ferziger J.H. (ed.) Large Eddy Simulation, Chap. 3, ICASE/LaRC Series in Computational Science and Engineering, pp. 109–154 (1996)
12. Geurts, B.J.: Inverse modeling for large-eddy simulation. Phys. Fluids **9**(12), 3585–3587 (1997)
13. Geurts, B.J., Fröhlich, Y.: A framework for predicting accuracy limitations in large-eddy simulation. Phys. Fluids **14**(2), L41–L44 (2002)
14. Geurts, B.J.: Elements of Direct and Large-Eddy Simulation. Cambridge University Press, Cambridge (2004)
15. Itoh, M., Yamada, Y., Imao, S., Gonda, M.: Experiments on turbulent flow due to an enclosed rotating disc. In: Rodi W., Canic E.C. (eds.) Engineering Turbulence Modelling and Experiments, pp. 659–668. Elsevier, New York (1990)
16. Jacques, R., Le Quéré, P., private communication
17. Kaber, O.S.M.: A Legendre pseudo-spectral viscosity method. J. Comput. Phys. **128**(1), 165–180 (1995)
18. Karamanos, G.S., Sherwin, S.J., Morrison, J.: Large eddy simulation using unstructured spectral/*hp* elements. In: Second International Conference on Direct Numerical Simulation and Large Eddy Simulation, Rutgers, New Jersey (1999)
19. Karamanos, G.S., Karniadakis, G.E.: A spectral vanishing viscosity method for large-eddy simulation. J. Comput. Phys. **163**, 22–50 (2000)
20. Kirby, R.M., Karniadakis, G.E.: Coarse resolution turbulence simulations with spectral vanishing viscosity-large eddy simulation (SVV–LES). J. Fluids Eng. **124**(4), 886–891 (2002)
21. Kirby, R.M., Sherwin, S.J.: Stabilisation of spectral/*hp* element methods through spectral vanishing viscosity: application to fluid mechanics modeling. Comput. Methods Appl. Mech. Eng. **195**, 3128–3144 (2006)
22. Launder, B.E., Tselepidakis, D.P.: Application of a new second moment closure to turbulent channel flow rotating in orthogonal mode. Int. J. Heat Fluid Flow **15**, 2 (2004)
23. Lesieur, M., Métais, O., Comte, P.: Large-eddy simulations of turbulence. Cambridge University Press, Cambridge (2004)
24. Littell, H.S., Eaton, J.K.: Turbulence characteristics of the boundary layer on a rotating disc. J. Fluid. Mech. **266**, 175–207 (1994)
25. Lygren, M., Andersson, H.I.: Turbulent flow between a rotating and a stationary disc. J. Fluid. Mech. **426**, 297–326 (2001)
26. Lygren, M., Andersson, H.I.: Large eddy simulations of the turbulent flow between a rotating and a stationary disc. Z. Angew. Math. Phys. **55**, 268–281 (2004)
27. Maday, Y., Kaber, S.M.O., Tadmor, E.: Legendre pseudo-spectral viscosity method for nonlinear conservation laws. SIAM J. Numer. Anal. **30**(2), 321–342 (1993)
28. Pasquetti, R., Bwemba, R.: A spectral algorithm for the Stokes problem in vorticity-vector potential formulation and cylindrical geometry. Comput. Methods Appl. Mech. Eng. **117**, 71–90 (1994)
29. Pasquetti, R., Xu, C.J.: High-order algorithms for large eddy simulation of incompressible flows. J. Sci. Comput. **17**(1–4), 273–284 (2002)
30. Pasquetti, R.: High-order LES modeling of turbulent incompressible flows. C.R. Acad. Sci. Paris **333**, 39–49 (2005)
31. Pasquetti, R.: Spectral vanishing viscosity method for LES: Sensitivity to the SVV control parameters. J. Turbulence **6**(N12), Special issue: Marseille Euromech Colloquium (2005)
32. Pasquetti, R.: Spectral vanishing viscosity method for large eddy simulation of turbulent flows. J. Sci. Comp. **27**(1–3), 365–375 (2006)
33. Pasquetti, R.: Spectral Vanishing Viscosity Method for High-Order LES: Computation of the Dissipation Rates. In: ECCOMAS CFD 2006 Congress, Egmond aan Zee, Holland, 5–8 September 2006
34. Pasquetti, R., Bwemba, R., Cousin, L.: A pseudo-penalization method for high Reynolds number unsteady flows. Appl. Numer. Math. (On line)
35. Patera, A.T., Orszag, S.A.: Instability of pipe flow. In: Nonlinear Problems: Present and Future, North-Holland, Amsterdam (1982)
36. Piomelli, U., Balaras, E.: Wall-layer models for large-eddy simulations. Annu. Rev. Fluid Mech. **34**, 349–374 (2002)
37. Poncet, S., Chauve, M.P., Schiestel, R.: Batchelor versus stewartson flow structures in a rotor–stator cavity with throughflow, Phys. Fluids **17**(7), 075110 (2005)
38. Raspo, I., Hugues, S., Serre, E., Randriamampianina, A., Bontoux, P.: Spectral projection methods for the simulation of complex three-dimensional rotating flows. Comput. Fluids **31**(4-7), 745–767 (2002)

39. Sagaut, P.: Large-Eddy Simulation for Incompressible Flows: An Introduction. Scientific Computation Series, Springer, Heidelberg (2005)
40. Schouveiler, L., Le Gal, P., Chauve, M.P., Takeda, Y.: Spiral and Circular waves in the flow between a rotating and a stationary disc. Exp. Fluids **26**, 179–187 (1999)
41. Serre, E., Crespodel Arco, I., Bontoux, P.: Annular and spiral patterns in flows between rotating and stationary discs. J. Fluid. Mech. **434**, 65–100 (2001)
42. Serre, E., Tuliska-Sznitko, E., Bontoux, P.: Coupled theoretical and numerical study of the flow transition between a rotating and a stationary disc. Phys. Fluids **16**(3), 688–706 (2004)
43. Serre, E., Pulicani, J.P.: 3D pseudo-spectral method for convection in rotating cylinder. Comput. Fluids **30**(4), 491–519 (2001)
44. Séverac, E., Serre, E., Bontoux, P.: A spectral vanishing viscosity technique as large eddy simulation of transitional rotor–stator flows. ETC6 Congress, Lille (2005)
45. Stolz, S., Adams, N.A.: An approximate deconvolution procedure for large-eddy simulation. Phys. Fluids **11**(7), 1699–1701 (1999)
46. Stolz, S., Adams, N.A., Kleiser, L.: An approximate deconvolution model for large-eddy simulation with application to incompressible wall-bounded flows. Phys. Fluids **13**(4), 997–1015 (2001)
47. Tadmor, E.: Convergence of spectral methods for nonlinear conservation laws. SIAM J. Numer. Anal. **26**(1), 30–44 (1989)
48. Wu, X., Squires, K.D.: Prediction and investigation of the turbulent flow over a rotating disc. J. Fluid. Mech. **418**, 231–264 (2000)
49. Xu, C.J., Pasquetti, R.: Stabilized spectral element computations of high Reynolds number incompressible flows. J. Comput. Phys. **196**(2), 680–704 (2004)